Available online at www.sciencedirect.com

jmr&t Journal of Materials Research and Technology

www.jmrt.com.br

Original Article

Manufacturing optimisation of an original nanostructured (beta + gamma)-TiNbTa material

Cristina García-Garrido[a], Carlos Gutiérrez-González[b], Ramón Torrecillas[c], Luis Pérez-Pozo[d], Christopher Salvo[e], Ernesto Chicardi[f,*]

[a] Instituto de Ciencia de Materiales de Sevilla (ICMSE-CSIC), Américo Vespucio 49, 41092 Sevilla, Spain
[b] Nanoker Research S.L. Polígono Industrial de Olloniego, parcela 22A, Nave 5, 33660 Oviedo, Asturias, Spain
[c] Centro de Investigación en Nanomateriales y Nanotecnología (CINN) [Consejo Superior de Investigaciones Científicas (CSIC), Universidad de Oviedo, Principado de Asturias], Avda. de la Vega, 4–6, 33940 El Entrego, Spain
[d] Department of Mechanical Engineering, Universidad Técnica Federico Santa María, Av. España 1680, Casilla 110-V, Valparaíso, Chile
[e] Advanced Ceramics and Nanotechnology Laboratory, Department of Materials Engineering, Faculty of Engineering, University of Concepcion, Concepcion, Chile
[f] Departamento de Ingeniería y Ciencia de los Materiales y del Transporte, Escuela Politécnica de Sevilla, Universidad de Sevilla (EPS-US), C/ Virgen de África 7, 41011 Sevilla, Spain

ARTICLE INFO

Article history:
Received 8 October 2018
Accepted 12 March 2019
Available online 27 May 2019

Keywords:
Ti alloys
TiNbTa alloys
Mechanical alloying
Nanostructured materials
Pulsed electric current sintering
Biaxial stress

ABSTRACT

An original (beta + gamma)-TiNbTa material was manufactured by an optimised powder metallurgy treatment, based on a mechanical alloying (MA) synthesis, carried out at low energy, and a subsequently field assisted consolidation technique, the pulsed electric current sintering (PECS). The successful development of this (beta + gamma)-TiNbTa material was possible by the optimisation of the milling time (60 h) for the MA synthesis and the load and sintering temperature for the PECS (30 MPa and 1500 °C), as key parameters. Furthermore, the selected heating and cooling rates were 500 °C min^{-1} and free cooling, respectively, to help maintain the lowest particle size and to avoid the formation of a detrimental high stiffness, hexagonal (alpha)-Ti alloy. All these optimised experimental conditions enabled the production of a full densified (beta + gamma)-TiNbTa material, with partially nanostructured areas and two TiNbTa alloys, with a body centred cubic (beta) and a novel face-centred cubic (gamma) structures. The interesting microstructural characteristics gives the material high hardness and mechanical strength that, together with the known low elastic modulus for the beta-Ti alloys, makes them suitable for their use as potential biomaterials for bone replacement implants.

* Corresponding author.
E-mail: echicardi@us.es (E. Chicardi).
https://doi.org/10.1016/j.jmrt.2019.03.004

1. Introduction

Nanostructured materials (NSMs) are attracting a great interest thanks to their improved properties in comparison with coarse-grained materials [1–3]. They show higher diffusivity, greater corrosion resistance [4], magnetic behaviour [5], reduced sintering temperature, catalytic properties, higher hardness, fracture strength and yield strength. Conversely, they present lower ductility and similar elastic modulus [6–8]. The lower ductility can be resolved by the design of materials with bimodal grain size distribution, i.e., nanoparticles embedded into the microparticles [9].

NSMs have a wide range of potential applications. As example, nanometric diatomaceous earth, carbon, zeolites, lime and clays, are used as adsorbent materials to remove contaminants [10] and as catalytic materials, accelerating the naphtha reforming and cracking chemical reactions [11]. Fe-based nanoparticles are used to remove water pollutants including halogenated organic compounds (HOCs) [12] and heavy metals [13]. For biomedical applications, NSMs are used in tissue engineering, biomimicry, scaffolds, bioprobe, biomarkers, cancer diagnosis and localised drug delivery for tumour treatment, amongst others [14–18].

For bone tissue engineering, NSMs are interesting due to their superior strength. This characteristic allows for the production of porous materials (foams) of β-Ti alloys, which are currently being developed for this purpose, with their improved mechanical strength [11,19,20] and without the detrimental effect of the diminished yield and fracture strengths caused by the porosity.

These β-Ti alloys, with body centred cubic (bcc) structure and low stiffness, are replacing the usual high stiffness commercially pure Ti and the Ti6Al4V alloy, with hexagonal close-packed (hcp) structure, that causes *stress-shielding* [21]. This phenomenon is a direct consequence of the incorrect load transference from the implant to the bone that causes the loosening of the implant and/or premature bone fracture. These alloys are produced by the addition of β-stabiliser elements, such as Mo, Nb and Ta, that assist in the maintenance of the beta structure of Ti at room temperature [11]. Amongst these additions, Nb and Ta have particularly relevance, due to their ability to help improve the Ti alloys biocompatibility [22–24].

The different methods to produce NSM are based on two approaches, the "bottom-up", in which bulk nanostructured materials are assembled from individual atoms or nanoparticles (chemical and physical vapour depositions (CVD and PVD) [25,26], electrodeposition [27], etc.), and the "top–down", in which coarse-grained materials are processed to refine the grains, yielding the desired nanostructures [28]. Processes used include etching [29,30], powder metallurgy (PM) [31,32] and equal-channel angular pressing (ECAP) [33].

One interesting way to produce the nanostructured β-Ti alloys for bone tissue engineering, with an expected improved yield strength and hardness, could be their synthesis by powder metallurgy mechanical alloying (MA) and their consolidation by a suitable thermal treatment. The MA is an effective technique to produce non-thermodynamic equilibrium alloys with an extension of the solubility limits, amorphous alloys and metastable and nanocrystalline phases [32,34]. However, this way has only been used to develop nano Ti and nano Ti–6Al–4V alloys [35–37], with improved strength but a total absence of the β structure and, consequently, with a high elastic modulus due to their α (hcp) structure [20], and so not an appropriate material to avoid the *stress-shielding* phenomenon.

In addition, another important problem in the development of bulk-nanostructured materials by PM is the grain growth that takes place during the thermal consolidation [38]. Thus, to maintain the nanostructure, it is necessary to apply a fast sintering process. For this purpose, Electric Field Assisted Sintering Techniques (FAST) seems to be ideal due to the short time that the consolidation process takes. As an example, a consolidation process by Pulsed Electric Current Sintering (PECS) can take a number of minutes [39] whereas Capacitor Discharge Sintering (CDS) can consolidate materials in a matter of milliseconds [40]. Nevertheless, finding the most favourable conditions to reach a fully dense material, with the optimal mechanical properties, nanostructure and preserving the initial phases, is not an easy task. It is necessary to optimise mainly the applied pressure, the sintering temperature and the heating and cooling rates [41–43].

Therefore, taking into account all the above mentioned aspects, this work is focused on the development of a TiNbTa material as a potential biomaterial for biomedical applications by MA and subsequently PECS, adjusting the sintering conditions to obtain full densification, the lowest possible particle size, optimal mechanical properties, homogenisation of Ti, Nb and Ta and with total absence of the detrimental high stiffness hcp (α) structure.

2. Experimental procedure

Titanium (99.6% purity, <325 mesh), niobium (99.9% purity, <325 mesh), and tantalum (99.9% purity, <325 mesh), supplied by Noah Tech (San Antonio, TX, USA) were used to develop a 57Ti–30Nb–13Ta (at.%) material (henceforth referred to as TiNbTa).

The TiNbTa synthesis was carried out by MA at low energy to produce the total alloying of the element but preventing any excessive grain growth. A PM400 (Retsch GmbH) planetary ball mill was used at a spinning rate of 250 rpm for the main plate and the two vials, under an inert atmosphere (Argon, by Linde Group, Spain, with H_2O ≤8 ppm and O_2 ≤2 ppm). The milling media used was yttria stabilised zirconia (YSZ) for both the balls and vials. A ball-to-powder ratio (BPR) of 10 was used. 3 wt.% of zinc stearate (NOAH tech, 99.9% purity, <325 mesh) was also introduced as process control agent (PCA) to avoid excessive welding and the agglomeration of particles. The powder mixtures were milled between 1 h and 120 h, at cyclic intervals of 30 min OFF-30 min ON, to avoid any excessive increase of temperature inside the vials.

Subsequently, the as-synthesised TiNbTa material, named as *p*TiNbTa*x*h (being *p* from powders and *x* the hours of milling time), was sintered by PECS (FCT System GmbH, Germany, Model HPD-25) at temperatures and pressures between 1300 °C and 1500 °C and 30–60 MPa, respectively, at a high heating rate of 500 °C min^{-1} with a dwell time of 10 s and subsequent free cooling, in order to find the optimised sintering conditions,

and to study the microstructural evolution. A medium vacuum (10^{-3} atm) was used as a work atmosphere. The temperature was measured by an infrared pyrometer coupled to the PECS. The powders were place inside the mould and coated with graphite paper in order to avoid their release from the mould during sintering. Thus, the as-sintered TiNbTa specimens, named as x°C_yMPa (where x is the sintering temperature and y the applied pressure), were prepared with a geometry of 20 mm in diameter and 10 mm in height.

The X-Ray Diffraction (XRD) patterns for the as-synthesised and the as-sintered TiNbTa specimens, after the metallographic treatment, i.e., cutting and surface polishing (P400 grit SiC, diamond suspensions with particles of 9 μm, 3 μm, 1 μm and, finally, a colloidal suspension of 0.05 μm of SiC particles), were collected by a PANalytical X'Pert Pro instrument equipped with a Bragg–Brentano $\theta/2\theta$ geometry detector, a Cu Kα radiation source (40 kV, 40 mA), a secondary Kα filter, and an X'Celerator detector. They were obtained by scanning from 2θ between 20° and 140° with a step of 0.02° and a counting time of 300 s step^{-1}. Lanthanum hexaboride, LaB_6 (Standard Reference Material 660b, NIST), was used as internal pattern to calibrate the positions of the diffraction lines. The structural elucidations of the phases and the space group symmetries (SGS) were determined by the DICVOL software, using the dichotomy method [44], and compared with the Crystallography Open Database (COD).

Secondary scanning electron microscopy (SEM) images were obtained, using a Hitachi S-4800 field emission at an acceleration voltage of 5 kV, on the as-synthesised and the as-sintered TiNbTa specimens. The punctual quantifications and mappings of Ti, Nb and Ta were carried out in each phase by point X-Ray Energy Dispersive Spectrometry (EDS) with a detector coupled in the SEM at an acceleration voltage of 30 kV. Image analysis (IA) with the Image-Pro Plus 6.2 software was employed to obtain the particle size distribution from the SEM micrographs using the linear intercept method [45]. Five SEM micrographs at magnifications of 5kx and 10kx were used per each TiNbTa specimen.

Vickers hardness (VH) tests were performed at room temperature in a microhardness FM-700 instrument (Future-Tech. Corp.) at a load of 9.81 N (1 kgf) for 15 s. 100 microindentations were randomly taken, on each as-sintered TiNbTa specimen, to obtain the VH distributions and the reported value was the average of the different measurements. A carefully polishing process was carried out before to Vickers tests to avoid any influence from surface roughness. Furthermore, another 20 VH tests were carried out, in each specific area, to determine the hardness of different zones found in the as-sintered TiNbTa specimens.

Finally, the flexural strength was measured using the ball on three balls test (B3B-test), where a disc specimen was supported on three balls and loaded symmetrically by the fourth ball. The diameters of the four balls were 3 mm. Additional details about this mechanical test can be found elsewhere [46]. The tensile-loaded surfaces of the B3B specimens (disks with a thickness of 1 mm and a diameter of 12 mm) were ground and polished to avoid surface damage. The tests were performed using an electromechanical universal testing machine at room temperature and under load rate of 100 N s^{-1}. The fracture load was used to calculate the maximum flexural strength (σ_{max}) by the Börger equation [47]. Five specimens were evaluated for each as-sintered TiNbTa specimen.

3. Results and discussion

3.1. *Microstructural characterisation of the as-synthesised TiNbTa*

The XRD patterns for the as-synthesised TiNbTa are shown in Fig. 1a. For the pTiNbTa1h, the peaks corresponding to the raw transition metals were detected, specifically, Ti (*hcp* structure and *P63/mmc* SGS), Nb (*bcc* structure, and *Im3m* SGS) and Ta (*bcc* structure and *I-43 m* SGS), and indexed according to the COD reference patterns no. 1532765, 1539041 and 1541266, respectively. When the milling time was increased up to 60 h, two different phases were detected. They were a face-centred cubic (fcc) and a body-centred cubic (bcc) phase with *Fm3m* and

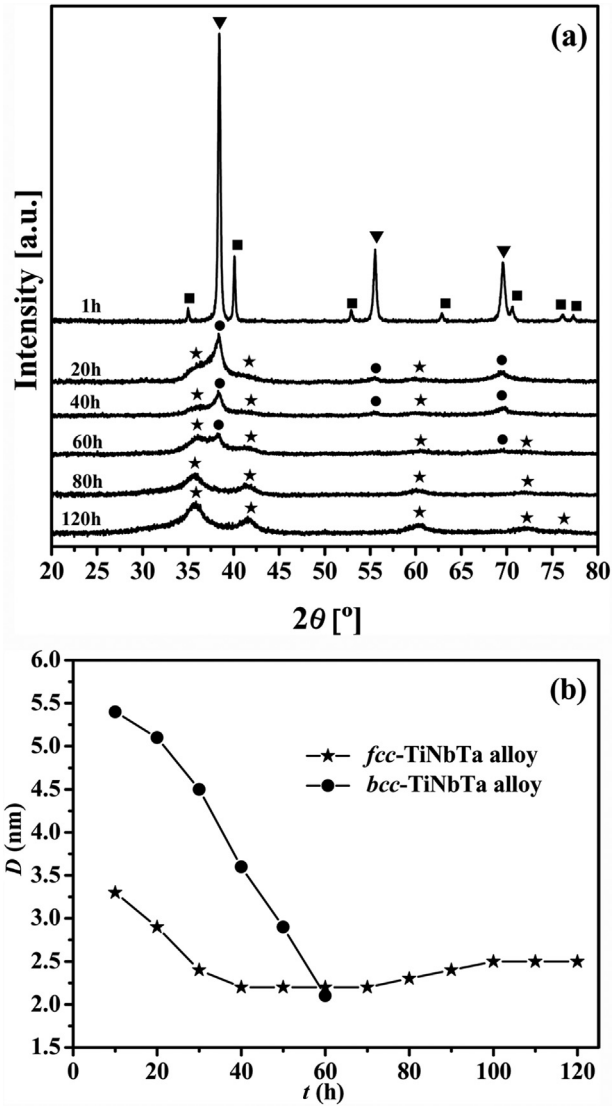

Fig. 1 – (a) XRD patterns for the pTiNbTa milled between 1 h and 120 h. (■) hcp-Ti; (▼) bcc-Nb and bcc-Ta; (●) bcc-TiNbTa alloy; (⋆) fcc-TiNbTa alloy. (b) Crystalline domain size (*D*) determined for both (●) bcc-TiNbTa and (⋆) fcc-TiNbTa alloy.

Im3m SGS, respectively. These phases were indexed according to the reference patterns no. 1534903 (fcc-Nb type) and 4000948 (bcc-Nb type) in the COD, respectively. Subsequently, from 80 h to 120 h of milling time, only the fcc phase was detected. This suggests a metastable character of the bcc phase that changes to a stable fcc phase thanks to the energy transferred by the milling process. Finally, no Zr phases were found, suggesting a low contamination from the milling media.

The determination of lattice parameters for both bcc and fcc phases showed similar values for all milling times, according to the low standard deviation obtained (3.308 ± 0.002 Å and 4.361 ± 0.002 Å for the bcc and fcc phases, respectively). This aspect suggests a similar composition for all milling times. The displacements of those lattice parameters with the corresponding references ($a = b = c = 3.301$ Å for bcc-Nb and $a = b = c = 4.230$ Å for fcc-Nb) together with the total absence of the Ti, Nb and Ta raw elements, suggests a total conversion of them. Thus, both fcc and bcc phases must be fcc-TiNbTa and bcc-TiNbTa alloys. This assertion is further corroborated later.

Fig. 1b shows the crystal domain size (D) determined by the Scherrer's equation [48] for both bcc and fcc TiNbTa alloys. The low intensity, and number of peaks, made impossible to apply the Williamson–Hall or Warren Averbach methods, where a family of peaks are necessary [49,50]. A general decreasing trend of D for both bcc and fcc TiNbTa alloys was observed with the increasing milling time up to 60 h. After this time, the D values remained practically invariant. The lowest D was reached for both alloys at 60 h of milling time (around 2.2 nm).

For the subsequent consolidation stage of the as-synthesised pTiNbTa, the specimen of pTiNbTa60h, with both bcc and fcc TiNbTa phases, and the lowest D, was selected to determine the evolution of the composition and microstructures.

3.2. *Pulsed electric current sintering process*

The as-synthesised pTiNbTa60h was sintered at four temperatures, two load pressures and fixed heating rate (Table 1). Fig. 2 shows the PECS applied programme (sintering temperature, load and shrinkage rates). It can be seen how the maximum sintering temperature (dotted red line) was reached after ~4 min of the PECS process. Also, for the 1300 °C_30 MPa, 1400 °C_1300 MPa and 1500 °C_30 MPa specimens, the temperature increased when the maximum pressure was attained. For the specimen with the double pressure applied, 1500 °C_60 MPa, preliminary tests, based on the first application of 60 MPa before the heating, produced the release of the powders from the graphite die. For that reason, it was decided to use the same condition for the sintering as used for the other three specimens. The maximum loads were maintained until the end of the shrinkage. Thus, from Fig. 2 it can be seen how the experimental heating rate reached the 500 °C min^{-1}, initially programmed.

In addition, the experimental cooling rate for the four specimens could be calculated from the PECS sintering curves (Table 1). They were around 300 °C min^{-1} for all specimens. However, considering the observed behaviour from the sintering temperature to approximately 900 °C (this temperature value was selected for all specimens in order to compare them), the cooling rate was around 600–700 °C min^{-1}. This high cooling rate, together with the high heating rate and only 10 s of dwell time, allowed the partial maintenance of the nanostructured characteristics for the as-sintered TiNbTa specimens, as will be evidenced later.

Looking at the shrinkage rate curve (continuous green lines in Fig. 2), three different peaks can be seen for all the as-sintered TiNbTa specimens. A first stage, around 1 min of the PECS progress, was associated with the compaction process due to the load application. Subsequently, during the heating stage, the second peaks are associated with the neck formation between particles and the porosity annihilation (sintering stage) [51]. A particular behaviour was observed for the specimen 1500 °C_60 MPa. In this case, two shrinkage peaks were detected in the heating rate zone. The second one is attributable to a partial formation of a liquid phase, due to the increase of the applied pressure. The combination of high heating rate and high pressure may lead to small temperature inhomogeneities in the sample, leading to melting of some specific zones of the disk. Finally, when the PECS progresses to the cooling rate stage, a third peak for all specimens appears. This third stage is associated with the thermal contraction as consequence of the abrupt decrease of temperature, from sintering temperature down to 400 °C. Following this third peak, no other phenomena were observed in the shrinkage curves of the different specimens up to the end of the PECS. It is important to emphasise that only when the sintering peak (second stage) reached the shrinkage value of 0, was the PECS process forced to go to the cooling rate stage. Thus, the dwell time necessary was around 10 s for all specimens, as shown in Table 1.

3.3. *Microstructural characterisation of the as-sintered TiNbTa specimens*

The density of the as-sintered TiNbTa was measured by both geometry and by the Archimedes methods (Table 2). By both methods, increased values of absolute density were obtained with the sintering temperature between 1300 °C and

Table 1 – Sintering conditions used for the as-synthesised pTiNbTa60h. ST, sintering temperature; SP, sintering pressure; HR, heating rate; Dt, dwell time; CR, cooling rate, determined from ST to 900 °C and from ST to 400 °C.

Specimen	ST (°C)	SP (MPa)	HR (°C min^{-1})	Dt (s)	CR, ST-900 °C (°C min^{-1})	CR, ST-400 °C (°C min^{-1})
1300 °C_30 MPa	1300	30	500	10	680	330
1400 °C_30 MPa	1400	30			570	300
1500 °C_30 MPa	1500	30			570	340
1500 °C_60 MPa	1500	60			580	300

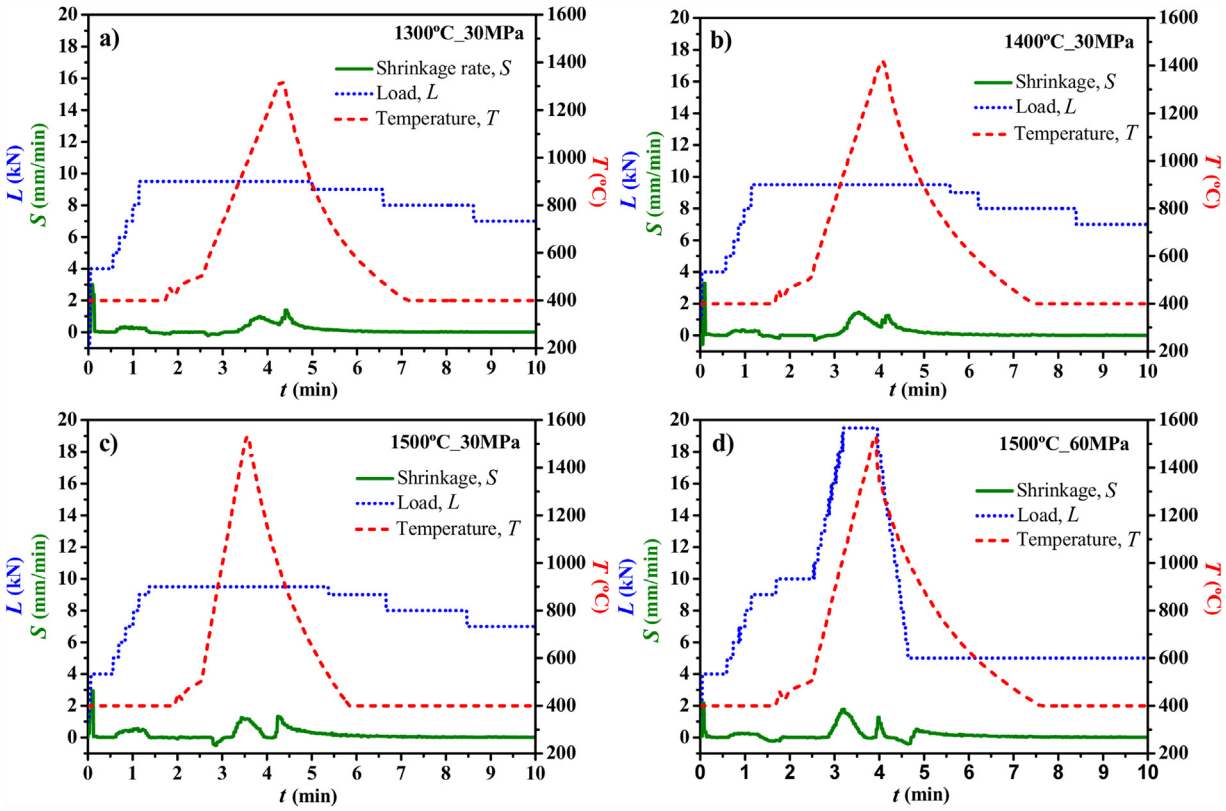

Fig. 2 – PECS curves for the as-synthesised pTiNbTa60h sintered at different pressure and temperature, showing the evolution of the applied load (*L*, dotted lines), sintering temperature (*T*, dashed lines) and shrinkage (*S*, continuous lines).

Table 2 – Density (by geometry and Archimedes methods) and volumetric porosity (by image analysis) for the as-sintered TiNbTa specimens.

Specimen	Geometric density(g/cm^3)	Archimedes density(g/cm^3)	Volumetric porosity(%)
1300 °C_30 MPa	6.4	6.7	7.7
1400 °C_30 MPa	7.0	7.0	2.9
1500 °C_30 MPa	7.2	7.2	~0
1500 °C_60 MPa	7.2	7.1	~0

1500 °C. With an increase of pressure, from 1500 °C_30 MPa to 1500 °C_60 MPa, the density remained practically invariant. Therefore, according to the density measurements, the application of 1500 °C and 30 MPa is enough to obtain the maximum densification.

The XRD pattern for the as-sintered TiNbTa is illustrated in Fig. 3. The same fcc and bcc TiNbTa alloys were indexed (Fig. 3a). In this case, new slight peaks could be assigned to Yttrium Stabilized Zirconia (YSZ, reference pattern no. 9015117 of the COD [52]). Comparing the peak intensities, this contamination phase, coming from the milling media, seems to be in a low percentage.

On the other hand, the (111) and (110) reflections for both the fcc and the bcc TiNbTa alloys, respectively, underwent a 2θ displacement to higher values with the high energetic sintering conditions and also in comparison with the corresponding peaks of the as-synthesised pTiNbTa60 (Fig. 3a). This aspect suggests a decrease of the lattice parameters (according to Bragg's law) and therefore, a compositional variation for these phases during the PECS process. Both reflections remained displaced from the fcc-Nb and bcc-Nb reflections (shown as dotted lines in Fig. 3b for comparison purposes), suggesting that both phases remain as TiNbTa alloys. This assertion is further confirmed through the SEM–EDS results.

The volumetric porosity, distribution of phases and the particle morphology for the as-synthesised and the as-sintered TiNbTa specimens were determined from the SEM images (Figs. 4 and 5). It can be seen that the volumetric porosity, determined by the Image Analysis and according to the ASTM E2901 standard, showed an almost total absence of porosity for the highest sintering temperature 1500 °C (Table 2 and Fig. 4). This aspect is in accordance with the increase of density (Table 2).

For the pTiNbTa60h, agglomerated particles were observed which can be attributed to the ball milling process (Fig. 4). The particles that make up these agglomerations seem to be particles under micrometric sizes and with a close to spherical morphology. In turn, the SEM images for the TiNbTa specimens sintered at the lowest temperatures, i.e., 1300 °C_30 MPa and 1400 °C_30 MPa, show a heterogeneous microstructure formed

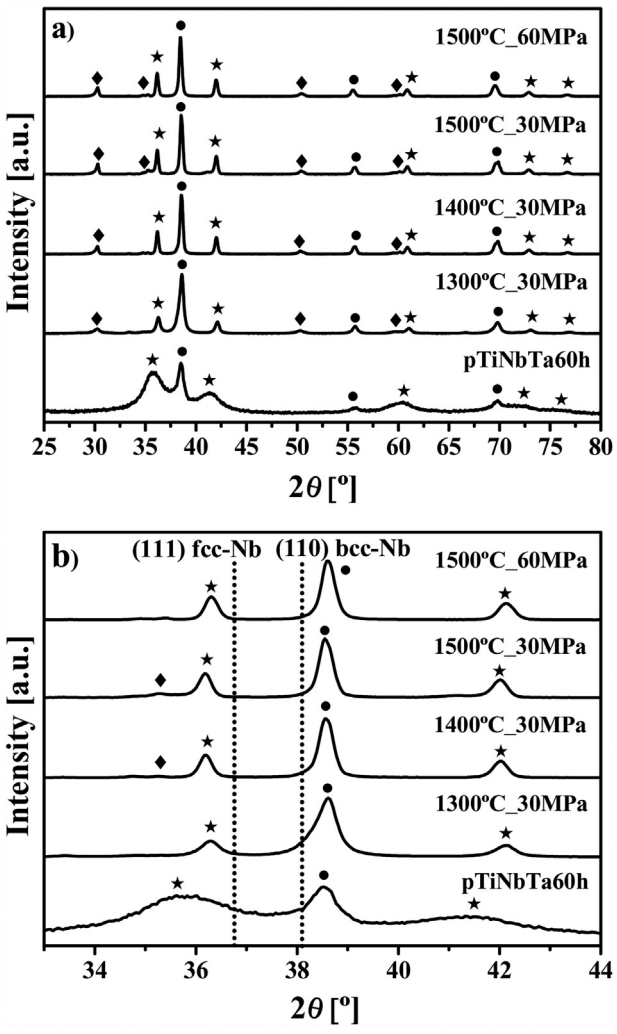

Fig. 3 – (a) XRD patterns for the as-sintered TiNbTa at different pressure and temperature. For comparison purpose, the XRD pattern for the pTiNbTa60h has also been displayed. (●) bcc-TiNbTa alloy; (⋆) fcc-TiNbTa alloy; (♦) YSZ. (b) Magnification of the same XRD patterns showing the 2theta displacements for the (111)-fcc and (110)-bcc peaks.

by three areas (marked as 1, 2 and 3 in Fig. 4). Two of these three areas are formed from nanometric particles (zones 1 and 2). When the sintering temperature was increased, i.e., for the 1500 °C_30 MPa and 1500 °C_60 MPa, the specimens evolved to more homogeneous microstructures, with only two different contrasting zones (1 and 2 in Fig. 4, where zone 1 corresponds to a nanostructured zone).

The SEM images at 10kX are shown in Fig. 5. It can be seen how the three zones observed in Fig. 4, for 1300 °C_30 MPa and 1400 °C_30 MPa correspond, in fact, to nanometric (zones 1 and 2) and submicrometric particles (zone 3) with different contrasts. Zone 3 shows dark particles and a grey continuous phase. On the other hand, the other two zones (zones 1 and 2) show three different contrasting regions for the nanoparticles (black, grey and white), possibly as consequence of different composition and structure (bcc and fcc phases). The specimens sintered at the highest temperature (1500 °C_30 MPa and 1500 °C_60 MPa) showed only two zones (zones 1 and 2 in Fig. 5). This suggests that at least two types of the particles have the same structure and the diffusion of Ti, Nb and Ta produced the homogenisation, since only two phases were detected by XRD (see Fig. 2). In addition, Fig. 5 also shows some clear particles (marked with dotted white squares) that can be assigned to the YSZ contamination.

General and points EDS–SEM were carried out to determine the composition of the different particles (Table 3 and Figs. 6 and 7). The general semi-quantitative EDS–SEM analysis, as determined by an average value of 20 measurements for each specimen, show similar TiNbTa compositions between the pTiNbTa60h and the as-sintered TiNbTa specimens. The zirconium atomic percentage, coming from milling media (YSZ), was around 5 at.% in all specimens. This is a lower amount in comparison with specimens where Hardened Stainless Steel was used as milling media [53]. On the other hand, the general TiNbTa composition, regardless of the Zr contamination, presented average atomic values close to the nominal 57Ti–30Nb–13Ta used.

In turn, the semi-quantitative point EDS–SEM analysis was carried out on all as-sintered TiNbTa specimens. It was impossible to discriminate between both fcc and bcc phases in the as-synthesised pTiNbTa60h due to the high level of particle agglomeration, so making it unfeasible to determine their composition. In addition, it is important to emphasise that it was only possible to measure the composition for the submicrometric particles area (Table 3). For the two nanostructured zones it was impossible to carry out accurate measurements due to their extremely low sizes (the lateral spread of X-ray is more than 2 μm for an accelerating voltage of 15 kV) [54–56]. Thus, in the dark particles of the measured zone, an increase of the Ti and Nb and a decrease of the Ta components was detected for the higher energetic sintering conditions, i.e., temperature and pressure. This contrasts with the bright particles of the same zone, where a decrease of Ti and an increase of Nb and Ta amounts were detected (Table 3). This fact suggests a trend to diffuse Ti, Nb and/or Ta during the sintering process to homogenise the phases when the temperature and the pressure were increased.

To corroborate the assertions about the composition of particles, representative EDS–SEM mappings were carried out in the submicrometric particle zone for the 1300 °C_30 MPa and 1500 °C_60 MPa specimens (Fig. 6). This zone shows both the determined Ti-rich dark phase and a Ti-poor bright phase, suggesting both phases correspond to the fcc and bcc TiNbTa alloys. Also, in some specimens small Zr-rich areas could be seen, corresponding to the YSZ particles from the milling media.

Also, representative EDS–SEM mappings for both nanoparticle zones were carried out on the specimen 1400 °C_30 MPa y 1500 °C_30 MPa (Fig. 7). The results showed similar behaviour to that of the submicrometric zone, where all the contrasts were TiNbTa alloys, with higher Ti amount for the darker contrast and higher Ta and Nb for the brighter contrasts. The Zr component due to the milling media was practically negligible in all the nanoparticle zones observed. Therefore, considering that for XRD only two alloys were detected (fcc and bcc TiNbTa), all these EDS–SEM mappings

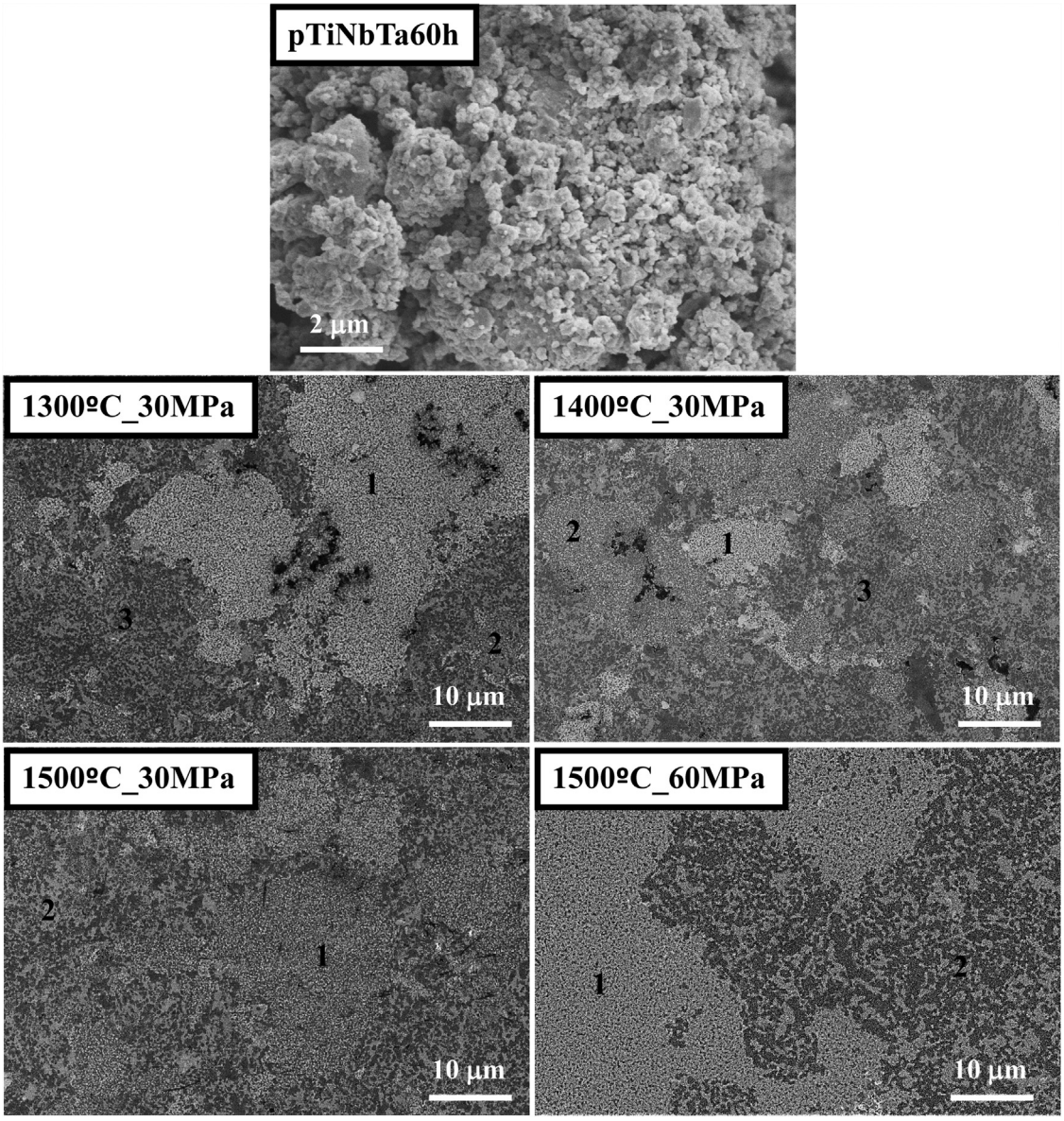

Fig. 4 – SEM images at 2kX for the as-synthesised pTiNbTa60h and the TiNbTa specimens after the PECS process.

and point EDS–SEM suggest that all dark and bright contrasts, found in the different zones, were the same phases, in this case, a fcc and a bcc TiNbTa alloy with different Ti–Nb–Ta compositions.

Average and distribution particle sizes were determined for the TiNbTa specimens by Image Analysis, according to the methods described earlier in the experimental section (Fig. 8 and Table 4). This clearly shows an increase of average particle size with an increase of sintering temperature, from 1300 °C to 1500 °C, going from 100 nm to 360 nm. In turn, when the sintering pressure was increased from 30 MPa to 60 MPa at 1500 °C, the average particle size also increased to 480 nm. This effect is a direct consequence of the formation of a melting metallic phase during sintering when the pressure was increased up to 60 MPa, as previously mentioned. In these conditions, the liquid phase causes an increment of the atomic diffusion driving force and, consequently, an increase of particle size.

The comparison of the 95 percentile, i.e., the value from which 95% of the particles are below, showed an increasing trend, from 260 nm to 970 nm, for 1300 °C_30 MPa and 1500 °C_60 MPa, but always in the submicrometric range. In addition, the two different populations of particle sizes, i.e., the nano- and the submicrometric-particles, could be distinguished except in the case of the 1300 °C_30 MPa, where a majority of nanometric particles were detected. Therefore, at this moment, it can be asserted that it was easy to get a full consolidation of a mixture of nano and submicrometric bcc + fcc TiNbTa alloys by PECS, even when high energetic sintering conditions (temperature and pressure) were applied.

3.4. *Mechanical behaviour*

To understand the effect of the microstructure evolution on the mechanical properties of the as-sintered TiNbTa

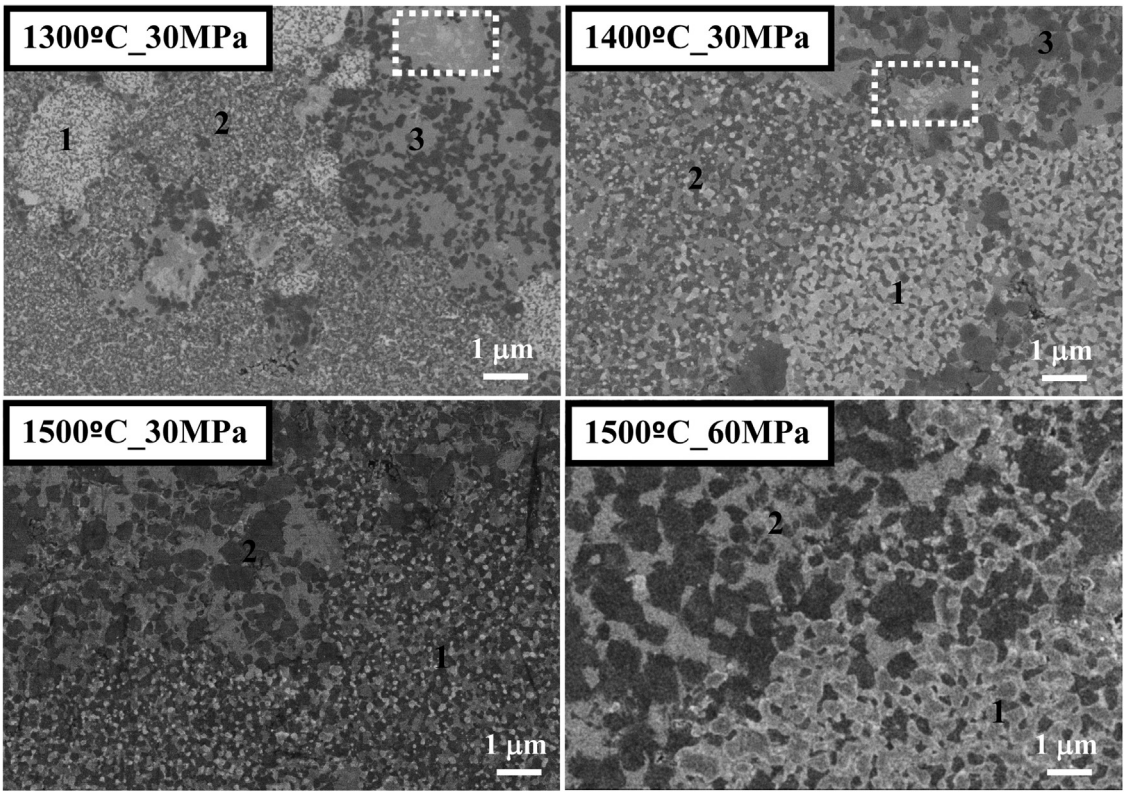

Fig. 5 – SEM images at 10kX for the as-synthesised pTiNbTa60h and the TiNbTa specimens after PECS process. YSZ particles are marked with dotted white squares.

Table 3 – General and points EDS–SEM measurements, in atomic percentage (at.%), for the pTiNbTa60h and the submicrometric area of the as-sintered TiNbTa specimens.

Specimen pTiNbTa60h	General Ti: 56.5 ± 2.1	Nb: 26.4 ± 1.6	Ta: 12.0 ± 0.8	Zr: 5.1 ± 1.4
	General	Point EDS (bright contrast)		Point EDS (dark contrast)
1300 °C_30 MPa	Ti: 56.6 ± 1.5 Nb: 27.4 ± 0.4 Ta: 11.7 ± 0.2 Zr: 4.3 ± 1.7	Ti: 10.6 ± 2.8 Nb: 16.1 ± 11.4 Ta: 73.3 ± 14.0		Ti: 87.6 ± 2.4 Nb: 10.0 ± 1.5 Ta: 2.4 ± 1.9
1400 °C_30 MPa	Ti: 57.0 ± 0.8 Nb: 26.8 ± 0.9 Ta: 11.2 ± 0.4 Zr: 5.0 ± 0.9	Ti: 29.3 ± 3.6 Nb: 37.3 ± 3.1 Ta: 33.3 ± 4.0		Ti: 81.3 ± 3.8 Nb: 12.2 ± 3.5 Ta: 6.5 ± 1.1
1500 °C_30 MPa	Ti: 56.4 ± 0.2 Nb: 27.4 ± 0.7 Ta: 11.4 ± 0.1 Zr: 4.8 ± 0.5	Ti: 36.8 ± 4.5 Nb: 46.3 ± 3.0 Ta: 16.9 ± 2.1		Ti: 75.5 ± 4.3 Nb: 17.0 ± 3.0 Ta: 7.5 ± 2.6
1500 °C_60 MPa	Ti: 56.2 ± 1.1 Nb: 26.6 ± 0.9 Ta: 11.6 ± 0.2 Zr: 5.6 ± 0.7	Ti: 38.9 ± 3.0 Nb: 48.8 ± 4.4 Ta: 12.3 ± 3.1		Ti: 72.6 ± 5.9 Nb: 19.3 ± 2.0 Ta: 8.1 ± 1.7

Energy-dispersive X-ray spectroscopy (EDS)-Scanning Electron Microscopy (SEM)

specimens, microhardness was first determined. After one hundred of tests, randomly carried out for each of the PECS conditions, the microhardness value distributions were obtained (Fig. 9 and Table 4). Initially, it was observed for the lower energetic sintering condition, i.e., 1300 °C_30 MPa, the lowest hardness (7.5 ± 1.6 GPa), as a consequence of the high remnant porosity, was measured (7.7 vol.%, Table 2). When the sintering temperature was increased for the 1400 °C_30 MPa specimen, the hardness increased until an average value of 9.7 ± 5.3 GPa. This increase it is clearly associated to the

Table 4 – Average (dav) and the percentile 95 (P95) particle size, the Vickers hardness carried out with a load of 1 kg (HV1), the ultimate biaxial strength (UBS) and the maximum strain (ε_{max}) for the as-sintered TiNbTa specimens.

Specimen	dav(nm)	P95(nm)	HV1(GPa)	UBS(MPa)	ε_{max}(%)
1300 °C_30 MPa	100	260	7.5 ± 1.6	73 ± 16	3.9 ± 1.2
1400 °C_30 MPa	280	580	9.7 ± 5.3	401 ± 27	11.5 ± 0.9
1500 °C_30 MPa	360	750	10.2 ± 4.7	459 ± 22	10.6 ± 0.6
1500 °C_60 MPa	480	970	9.2 ± 4.6	350 ± 15	10.5 ± 1.6

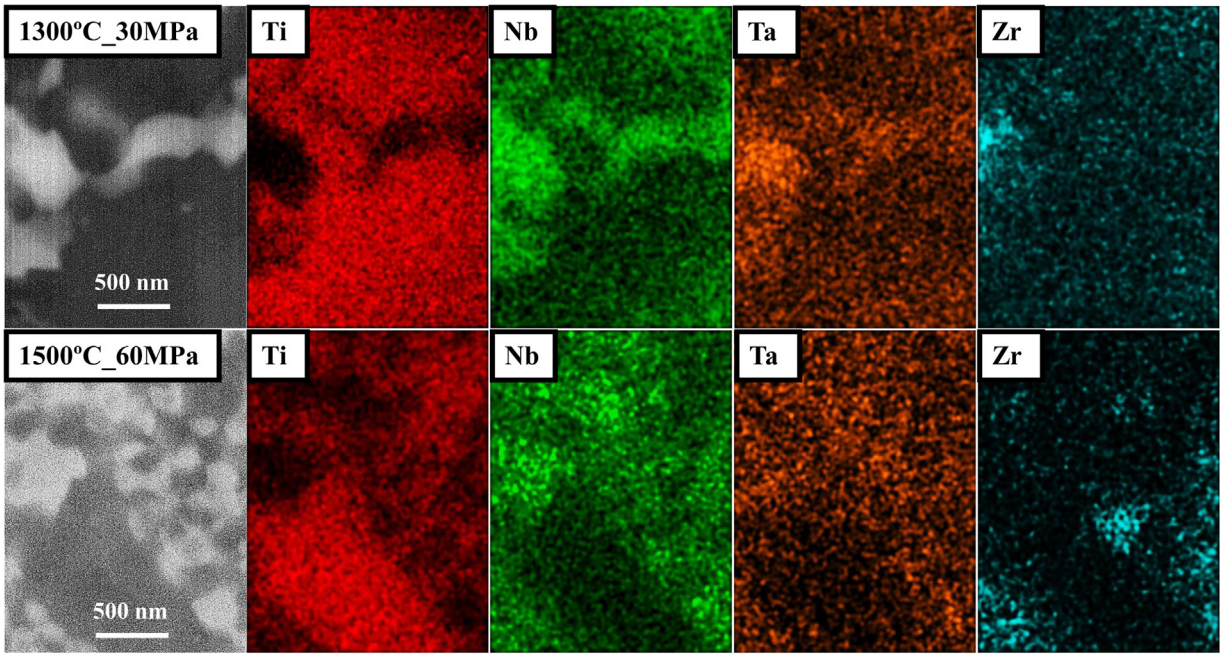

Fig. 6 – SEM–EDS mappings for the representative submicrometric and nanometric particle size areas of the 1300 °C_30 MPa and 1500 °C_60 MPa specimens, respectively.

abrupt decrease in porosity. However, the most important aspect observed for 1400 °C_30 MPa was the high distribution of microhardness values as shown by the high standard deviation. This aspect suggests different hardness for the three zones detected by SEM (Figs. 4 and 5). Finally, when the sintering temperature was increased until 1500 °C, specimens 1500 °C_30 MPa and 1500 °C_60 MPa, the measured hardness value was practically constant, with only a variation of around 5% (10.2 ± 4.7 GPa and 9.2 ± 4.6 GPa). For the 1500 °C_30 MPa, this slight increase was associated mainly with the total annihilation of porosity and, for the 1500 °C_60 MPa, when the sintering pressure was increased until 60 MPa, the slight diminishing of the microhardness was associated with the increase of average particle size until 480 nm (see Fig. 8). In addition, the decrease of standard deviation was associated to the of the microstructure from the three marked zones for the 1400 °C_30 MPa specimen to the two zones observed for 1500 °C_30 MPa and 1500 °C_60 MPa, as consequence of the increase of particle sizes and the homogeneity of composition. Thus, it is important to emphasise that to produce the desired microstructure, it is important to select the optimised sintering conditions by PECS and not only the decrease in porosity, which is normally used as a key characteristic parameter.

Considering the different zones observed, new microindentations were carried out in the three zones to determine their hardness values. The results obtained (Fig. 10) show how the nanometric zones presented higher hardness values (around 12 GPa) than the submicrometric zones (around 8 GPa), according to the Hall–Petch behaviour [57]. The detrimental low HV value of the nanostructured zones for the 1300 °C_30 MPa was as a consequence of the high porosity for this specimen. This is in accordance with the random study of the microhardness mentioned above.

Finally, the biaxial flexural strength was determined by 5 tests of each TiNbTa specimen (Fig. 11). This shows a representative stress–strain curve of the biaxial test for each specimen and Table 4 lists the average values. It can be seen that there is a low ultimate biaxial strength (UBS = 73 ± 16 MPa) for the 1300 °C_30 MPa. This reduction of the mechanical strength was again associated to the porosity that acts as a stress concentration factor. When the sintering temperature was increased, the biaxial strength reached the maximum value of 459 ± 22 MPa for the 1500 °C_30 MPa. This highest value is a direct consequence of the total annihilation of porosity and the low average particle size. Finally, for this same temperature and at 60 MPa of pressure, i.e., the 1500 °C_60 MPa, the increase of particle size gave a non-negligible decrease of UBS (350 ± 15 MPa). Therefore, according of the UBS values, the optimised sintering conditions by PECS was 1500 °C and 30 MPa, in agreement with the hardness values. On the other

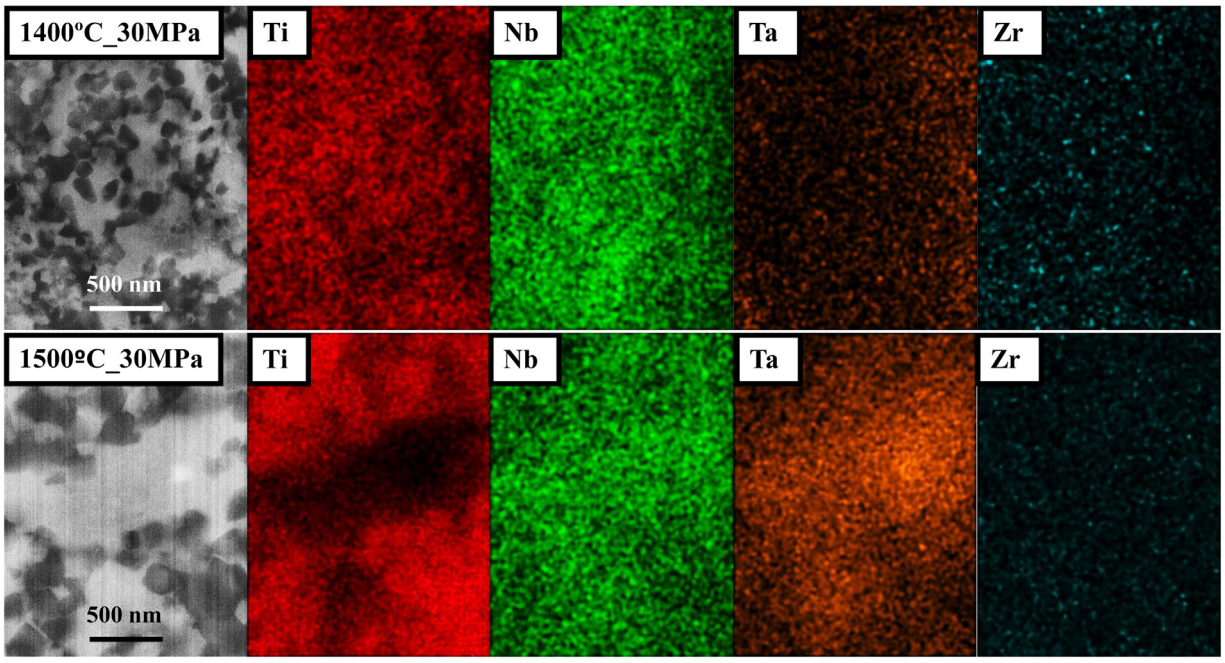

Fig. 7 – SEM–EDS mappings for the representative nanometric particle size areas of the 1400 °C_30 MPa and 1500 °C_30 MPa as-sintered TiNbTa specimens, respectively.

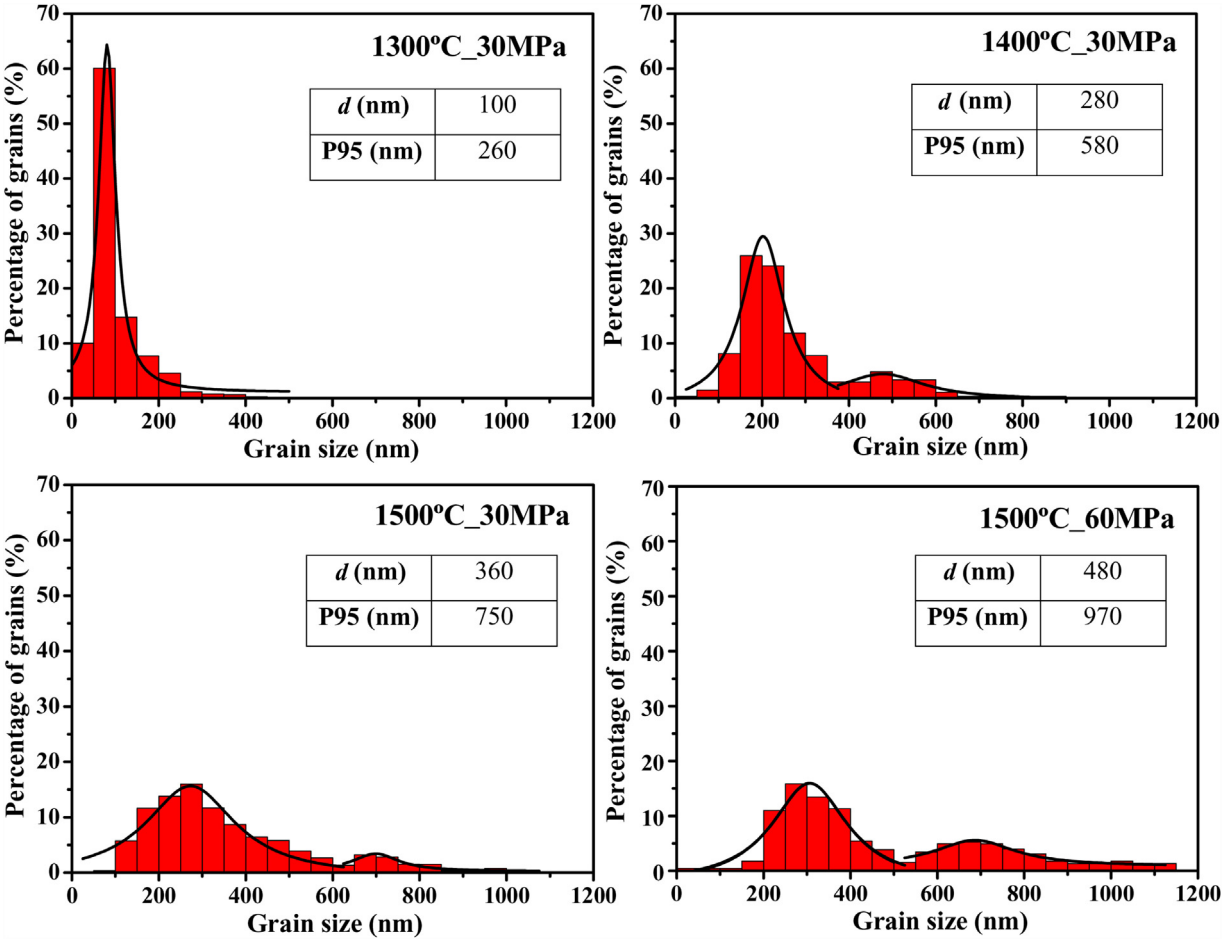

Fig. 8 – Average size and particle size distributions of the as-sintered TiNbTa specimens.

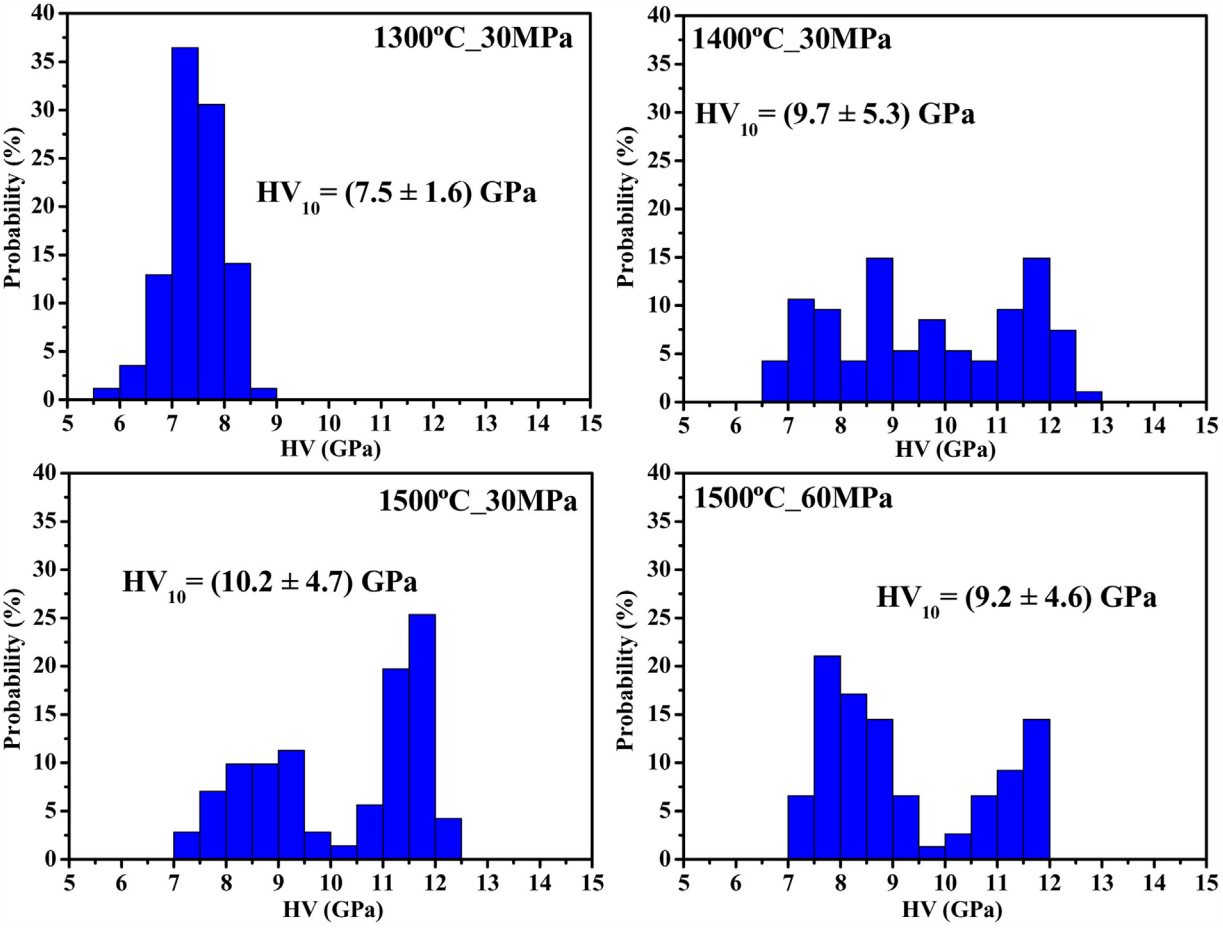

Fig. 9 – Vickers hardness (HV1) distributions of the as-sintered TiNbTa specimens.

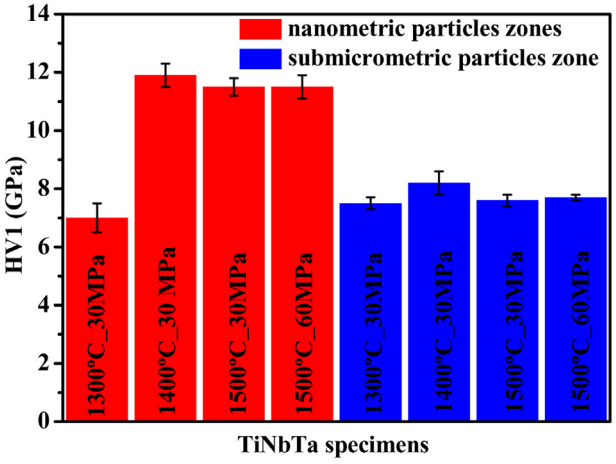

Fig. 10 – Discrimination of the Vickers hardness (HV1) for the submicrometric and nanometric particle size areas for the as-sintered TiNbTa specimens.

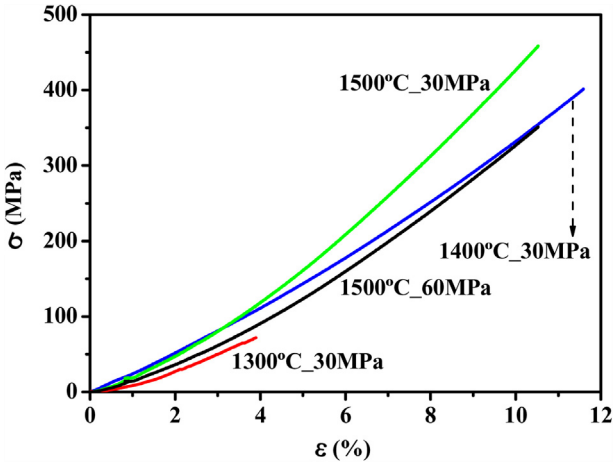

Fig. 11 – Stress–strain curve for the as-sintered TiNbTa specimens determined by the biaxial flexural tests.

hand, regarding the maximum strain, the ε values (Table 4) were between 10.5 and 11.5% for all specimens, except for the 1300 °C_30 MPa, where the porosity caused the fracture of the specimens before reaching the total strain level.

4. Conclusions

An interesting TiNbTa material with two different alloys, the usual body centred cubic (bcc or beta) structure and a novel face centred cubic (fcc or gamma) structure, was successfully

developed by a combined powder metallurgy method based on the synthesis by Mechanical Alloying (MA) at low energy and the consolidation by the Pulsed Electric Current Sintering (PECS).

The PECS process optimisation was based on the development of a TiNbTa material with full densification and nanostructured TiNbTa alloy. These characteristics were reached at a sintering temperature of 1500 °C and a load of 30 MPa. Lower temperatures (1300–1400 °C) and a higher pressure (60 MPa), caused higher porosity and the release of the powders from the die, respectively. Thus, these optimised conditions (1500 °C and 30 MPa), together with the high heating and cooling rates (500 °C min^{-1} and 900 °C min^{-1}, respectively) and the low dwell time (10 s) kept both (beta + gamma) partially nanostructured TiNbTa alloys.

The hardness and the maximum flexural strength for the (bcc + fcc)-TiNbTa material increased with the sintering temperature. The partial nanostructured zones presented higher hardness in comparison with the submicrometric zone. In addition, when the total annihilation of porosity was produced, with the application of more energetic sintering conditions (from 30 MPa to 60 MPa), this caused an increase of the particle size and a decrease of the hardness and flexural strength.

Therefore, the interesting microstructural characteristics that gives high hardness and mechanical strength to the material, together with the known low elastic modulus for the bcc-Ti alloys, makes the (beta + gamma)-TiNbTa materials suitable for their use as potential biomaterials for bone replacement foam implants.

Conflicts of interest

The authors declare no conflicts of interest.

Acknowledgments

The authors would like to thank the University of Seville for the use of its general research service (CITIUS) under the grant no. 2017/833 and to the Nanomaterials and Nanotechnology Research Centre (CINN-CSIC-UNIOVI) for the availability of the PECS device.

REFERENCES

[1] Gleiter H. Nanostructured materials: basic concepts and microstructure. Acta Mater 2000;48:1–29.
[2] Abraham AG, Manikandan A, Manikandan E, Jaganathan SK, Baykal A, Renganathan PS. Enhanced opto-magneto properties of $Ni_xMg_{1-x}Fe_2O_4$ ($0.0 \leq x \leq 1.0$) ferrites nano-catalysts. J Nanoelectron Optoelectron 2017;12:1326–33.
[3] Jacintha AM, Manikandan A, Chinnaraj K, Antony SA, Neeraja P. Comparative studies of spinel $MnFe_2O_4$ nanostructures: structural, morphological, optical, magnetic and catalytic properties. J Nanosci Nanotechnol 2015;15:9732–40.
[4] Saremi M, Yeganeh M. Improved corrosion resistance of nanostructured copper deposited by EB-PVD in acidic media. Int J Mod Phys: Conf Ser 2012;5:687–95.
[5] Suryanarayana C, Koch CC. Chapter 12: Nanostructured materials. In: Suryanarayana C, editor. Pergamon materials series. Pergamon; 1999. p. 313–44.
[6] Suryanarayana C. Recent developments in nanostructured materials. Adv Eng Mater 2005;7:983–92.
[7] Padmanabhan KA. Mechanical properties of nanostructured materials. Mater Sci Eng A 2001;304–306:200–5.
[8] Hahn H, Padmanabhan KA. Mechanical response of nanostructured materials. Nanostruct Mater 1995;6:191–200.
[9] Tian L, Li L. A review on the strengthening of nanostructured materials. Int J Curr Eng Technol 2018;8.
[10] Ellison DH. Handbook of chemical and biological warfare agents. 2nd ed. CRC Press; 2007.
[11] Niinomi M, Liu Y, Nakai M, Liu H, Li H. Biomedical titanium alloys with Young's moduli close to that of cortical bone. Regen Biomater 2016;3:173–85.
[12] Smith EH. Uptake of heavy metals in batch systems by a recycled iron-bearing material. Water Res 1996;30:2424–34.
[13] Gillham RW, O'Hannesin SF. Enhanced degradation of halogenated aliphatics by zero-valent iron. Groundwater 1994;32:958–67.
[14] du Toit LC, Kumar P, Choonara YE, Pillay V. 10 – Use of nanostructured materials in hard tissue engineering A2. In: Narayan R, editor. Nanobiomaterials. Woodhead Publishing; 2018. p. 257–95.
[15] Shi D, Gu H. Nanostructured materials for biomedical applications. Hindawi Publishing Corporation; 2008.
[16] Kikuchi A, Okano T. Nanostructured designs of biomedical materials: applications of cell sheet engineering to functional regenerative tissues and organs. J Control Release 2005;101:69–84.
[17] Tang Z, He C, Tian H, Ding J, Hsiao BS, Chu B, et al. Polymeric nanostructured materials for biomedical applications. Prog Polym Sci 2016;60:86–128.
[18] Rodzinski A, Guduru R, Liang P, Hadjikhani A, Stewart T, Stimphil E, et al. Targeted and controlled anticancer drug delivery and release with magnetoelectric nanoparticles. Sci Rep 2016;6.
[19] Ozaki T, Matsumoto H, Watanabe S, Hanada S. Beta Ti alloys with low Young's modulus. Mater Trans 2004;45:2776–9.
[20] Breme J, Eisenbarth E, Biehl V. Titanium and its alloys for medical applications. In: Titanium and titanium alloys. Wiley-VCH Verlag GmbH & Co. KGaA; 2005. p. 423–51.
[21] Ridzwan M, Shuib S, Hassan A, Shokri A, Ibrahim MM. Problem of stress shielding and improvement to the hip implant designs: a review. J Med Sci 2007;7:460–7.
[22] O'Brien B. Niobium biomaterials. In: Niinomi M, Narushima T, Nakai M, editors. Advances in metallic biomaterials: tissues, materials and biological reactions. Berlin, Heidelberg: Springer Berlin Heidelberg; 2015. p. 245–72.
[23] Leng YX, Chen JY, Yang P, Sun H, Wang J, Huang N. The biocompatibility of the tantalum and tantalum oxide films synthesized by pulse metal vacuum arc source deposition. Nucl Instrum Methods Phys Res Sect B: Beam Interact Mater At 2006;242:30–2.
[24] Matsuno H, Yokoyama A, Watari F, Uo M, Kawasaki T. Biocompatibility and osteogenesis of refractory metal implants, titanium, hafnium, niobium, tantalum and rhenium. Biomaterials 2001;22:1253–62.
[25] Bower C, Zhou O, Zhu W, Werder DJ, Jin SH. Nucleation and growth of carbon nanotubes by microwave plasma chemical vapor deposition. Appl Phys Lett 2000;77:2767–9.
[26] Singh J, Wolfe DE. Nano and macro-structured component fabrication by electron beam-physical vapor deposition (EB-PVD). J Mater Sci 2005;40:1–26.
[27] Vaezi MR, Sadrnezhaad SK, Nikzad L. Electrodeposition of Ni–SiC nano-composite coatings and evaluation of wear and

corrosion resistance and electroplating characteristics. Colloids Surf A: Physicochem Eng Asp 2008;315:176–82.
[28] Zhu YT, Lowe TC, Langdon TG. Performance and applications of nanostructured materials produced by severe plastic deformation. Scr Mater 2004;51:825–30.
[29] Cardinaud C, Peignon MC, Tessier PY. Plasma etching: principles, mechanisms, application to micro- and nano-technologies. Appl Surf Sci 2000;164:72–83.
[30] Chen Y, Xu P, Chen H, Li Y, Bu W, Shu Z, et al. Colloidal HPMO nanoparticles: silica-etching chemistry tailoring, topological transformation, and nano-biomedical applications. Adv Mater 2013;25:3100–5.
[31] Munir KS, Kingshott P, Wen C. Carbon nanotube reinforced titanium metal matrix composites prepared by powder metallurgy – a review. Crit Rev Solid State Mater Sci 2015;40:38–55.
[32] Suryanarayana C. Synthesis of nanocomposites by mechanical alloying. J Alloys Compd 2011;509:S229–34.
[33] Valiev RZ, Islamgaliev RK, Alexandrov IV. Bulk nanostructured materials from severe plastic deformation. Prog Mater Sci 2000;45:103–89.
[34] Suryanarayana C. Mechanical alloying and milling. Prog Mater Sci 2001;46:1–184.
[35] Falodun OE, Obadele BA, Oke SR, Maja ME, Olubambi PA. Synthesis of Ti–6Al–4V alloy with nano-TiN microstructure via spark plasma sintering technique. In: 4th international conference on mechanical, materials and manufacturing. Bristol: IOP Publishing Ltd.; 2017.
[36] Melnyk C, Weinstein B, Grant D, Gansert R, ASM International. Improved properties of light alloys (Ti-, Ti-alloys) using near-nano and nano-based materials for biomedical applications. Materials Park: ASM International; 2013.
[37] Ricceri R, Matteazzi P. Porous nano-crystalline Ti-alloy implants. Int J Powder Metall 2001;37:61–6.
[38] Fang ZZ, Wang H. Densification and grain growth during sintering of nanosized particles. Int Mater Rev 2008;53:326–52.
[39] Munir ZA, Anselmi-Tamburini U, Ohyanagi M. The effect of electric field and pressure on the synthesis and consolidation of materials: a review of the spark plasma sintering method. J Mater Sci 2006;41:763–77.
[40] Fais A. Processing characteristics and parameters in capacitor discharge sintering. J Mater Process Technol 2010;210:2223–30.
[41] Cuccu A, Montinaro S, Orru R, Cao G, Bellucci D, Sola A, et al. Consolidation of different hydroxyapatite powders by SPS: optimization of the sintering conditions and characterization of the obtained bulk products. Ceram Int 2015;41:725–36.
[42] Mondet M, Barraud E, Lemonnier S, Allain N, Grosdidier T. Optimisation of the mechanical properties of a Spark Plasma Sintered (SPS) magnesium alloy through a post-sintering in-situ precipitation treatment. J Alloys Compd 2017;698:259–66.
[43] Oke SR, Ige OO, Falodun OE, Obadele BA, Shongwe MB, Olubambi PA. Optimization of process parameters for spark plasma sintering of nano structured SAF 2205 composite. J Mater Res Technol 2018;7:126–34.
[44] Boultif A, Louer D. Powder pattern indexing with the dichotomy method. J Appl Crystallogr 2004;37:724–31.
[45] Thorvaldsen A. The intercept method—2. Determination of spatial grain size. Acta Mater 1997;45:595–600.
[46] Börger A, Supancic P, Danzer R. The ball on three balls test for strength testing of brittle discs: Part II: Analysis of possible errors in the strength determination. J Eur Ceram Soc 2004;24:2917–28.
[47] Börger A, Supancic P, Danzer R. The ball on three balls test for strength testing of brittle discs: stress distribution in the disc. J Eur Ceram Soc 2002;22:1425–36.
[48] Patterson AL. The Scherrer formula for X-ray particle size determination. Phys Rev 1939;56:978–82.
[49] Williamson GK, Hall WH. X-ray line broadening from filed aluminium and wolfram. Acta Metall 1953;1:22–31.
[50] Warren BE, Averbach BL. The effect of cold-work distortion on X-ray patterns. J Appl Phys 1950;21:595–9.
[51] Olevsky E, Froyen L. Constitutive modeling of spark-plasma sintering of conductive materials. Scr Mater 2006;55:1175–8.
[52] Howard CJ, Hill RJ, Reichert BE. Structures of ZrO_2 polymorphs at room temperature by high-resolution neutron powder diffraction. Acta Crystallogr Sect B 1988;44:116–20.
[53] Chicardi E, Garcia-Garrido C, Sayagues MJ, Torres Y, Amigo V, Aguilar C. Development of a novel fcc structure for an amorphous-nanocrystalline Ti–33Nb–4Mn (at.%) ternary alloy. Mater Charact 2018;135:46–56.
[54] Optimizing spatial resolution for EDS analysis. In: EDAX insight. 2011. p. 3.
[55] Probst C, Demers H, Gauvin R. Spatial resolution optimization of backscattered electron images using Monte Carlo simulation. Microsc Microanal 2012;18:628–37.
[56] Imeson D. On the spatial resolution of EDX composition determination. Ultramicroscopy 1982;9:307–10.
[57] Hansen N. Hall–Petch relation and boundary strengthening. Scr Mater 2004;51:801–6.